The Astrophysical Journal, 833:181 (12pp), 2016 December 20 doi:10.3847/1538-4357/833/2/181

CONSTRAINTS OF THE PHYSICS OF LOW-MASS AGB STARS FROM CH AND CEMP STARS

S. Cristallo[1,2], D. Karinkuzhi[3], A. Goswami[3], L. Piersanti[1,2], and D. Gobrecht[1,2]
[1] INAF—Osservatorio Astronomico di Teramo, I-64100, Italy
[2] INFN—Sezione di Perugia, Italy
[3] Indian Institute of Astrophysics, Koramangala, Bangalore 560034, India
Received 2016 September 12; revised 2016 October 10; accepted 2016 October 13; published 2016 December 16

ABSTRACT

We analyze a set of published elemental abundances from a sample of CH stars which are based on high resolution spectral analysis of ELODIE and SUBARU/HDS spectra. All the elemental abundances were derived from local thermodynamic equilibrium analysis using model atmospheres, and thus they represent the largest homogeneous abundance data available for CH stars to date. For this reason, we can use the set to constrain the physics and the nucleosynthesis occurring in low mass asymptotic giant branch (AGB) s.tars. CH stars have been polluted in the past from an already extinct AGB companion and thus show s-process enriched surfaces. We discuss the effects induced on the surface AGB s-process distributions by different prescriptions for convection and rotation. Our reference theoretical FRUITY set fits only part of the observations. Moreover, the s-process observational spread for a fixed metallicity cannot be reproduced. At $[Fe/H] > -1$, a good fit is found when rotation and a different treatment of the inner border of the convective envelope are simultaneously taken into account. In order to increase the statistics at low metallicities, we include in our analysis a selected number of CEMP stars and, therefore, we compute additional AGB models down to $[Fe/H] = -2.85$. Our theoretical models are unable to attain the large [hs/ls] ratios characterizing the surfaces of those objects. We speculate on the reasons for such a discrepancy, discussing the possibility that the observed distribution is a result of a proton mixing episode leading to a very high neutron density (the so-called i-process).

Key words: nuclear reactions, nucleosynthesis, abundances – physical data and processes – stars: chemically peculiar – stars: evolution – stars: low-mass

1. INTRODUCTION

CH stars are main sequence or giant stars showing a large variety of nuclear species. On their surfaces, in fact, the abundances of numerous heavy elements, normally attributed to the slow neutron capture process (the s-process), have been detected. Those elements cannot be produced in situ and, therefore, must have been accreted by already evolved companions. Best candidates are asymptotic giant branch (AGB) stars, which are responsible for the synthesis of the main component of the s-process (Gallino et al. 1998; Busso et al. 1999). Therefore, an observational study of CH stars could contribute to our knowledge of the physical processes at work in the internal layers of AGB stars. The structure of an AGB consists of an inert, partially degenerate CO core, surrounded by a He-shell, separated from an H-shell by a thin stellar layer (named He-intershell), and by a cool and extremely expanded convective envelope. During the AGB phase, the surface luminosity is mainly sustained by the H-burning shell. However, when its ashes reach high enough temperature and density, 3α reactions trigger a violent thermal runaway (thermal pulse, TP). The sudden energy release cannot be transported away radiatively and, therefore, convection mixes the whole He-intershell. As a consequence, the above layers (including the H-shell) expand and cool down. When convection ceases, the entropy barrier normally provided by the H-shell cannot prevent the penetration of the convective envelope in the underlying stellar region and, therefore, freshly synthesized nuclei are carried to the surface (third dredge up, TDU). Later, the H-shell switches on again and this cycle repeats, until the envelope is almost entirely lost via strong stellar winds. For a detailed description of AGB evolution see Herwig (2005), Straniero et al. (2006) and Karakas & Lattanzio (2014).

The main neutron source in AGB stars is the $^{13}C(\alpha, n)^{16}O$ reaction, which burns radiatively between two TPs (Straniero et al. 1995). The ^{13}C reservoir needed to reproduce observed distributions is stored in a tiny region below the formal border of the convective envelope, during TDU episodes. In that layer, a mechanism able to shape or stretch the sharp proton profile left by convection is required. Later, when the temperature rises again, those protons are captured by the abundant ^{12}C, leading to the formation of the so-called ^{13}C-pocket. The physics of such a mechanism is a highly debated subject and many hypotheses have been postulated: gravity waves plus Kelvin–Helmholtz instabilities (Battino et al. 2016), magnetic fields (Trippella et al. 2016), stochastic mixing events (Bisterzo et al. 2015), and ballistic plumes penetration (Cristallo et al. 2009b). Moreover, the possibility that other mechanisms, such as rotation, stretch the recently formed ^{13}C profile at a later time cannot be excluded (Piersanti et al. 2013).

In this paper, we compare a sample of CH stars, spanning over a large range of metallicities, with our AGB theoretical models. Rather than focusing on the comparison between each star with the corresponding model, we aim to verify if the treatment of the various physical processes in our models is accurate enough to allow the reproduction of the whole CH sample. In particular, we want to test if our theoretical recipe, to model the formation and evolution of the ^{13}C-pocket in AGB stars, is reliable or not. In Section 2 we present the observations and we discuss the errors affecting observational data. In Section 3 we describe our reference theoretical scenario used to interpret observations, and in Section 4 we compare it to data.

In Sections 5 and 6 we explore the consequences deriving from different prescriptions for convection and rotation on the theoretical interpretation of data. In Section 7 we extend our analysis to carbon enhanced metal poor (CEMP) stars. Finally, we deduce our conclusions in Section 8.

2. OBSERVATIONS

Program stars are selected from the CH star catalog of Bartkevicius (1996) and HES survey of Christlieb et al. (2001). The basic data of these objects along with the temperatures and radial velocities are listed in Goswami et al. (2006, 2016), Goswami & Aoki (2010), Karinkuzhi & Goswami (2014, 2015). The spectra for most of these objects are taken from the ELODIE archive (Moultaka et al. 2004). We have considered only those CH stars for which high resolution spectra are available in the archive with S/N >20. ELODIE is a cross dispersed echelle spectrograph used at the 1.93 m telescope of Observatoire de Haute Provence (OHP). Details about the spectrograph and reduction procedures are given in Baranne et al. (1996). The spectra recorded in a single exposure as 67 orders on a 1K CCD have a resolution of $R = 42{,}000$. The wavelength range spans from 3900 Å to 6800 Å. High-resolution spectra ($R \sim 50{,}000$) for a few objects HD 26, HD 5223, HD 198269, HD 224959, HD 209621, HE 1305+0007, and HE 1152-0355 were obtained using the High Dispersion Spectrograph attached to the 8.2 m Subaru Telescope (Noguchi et al. 2002). The observed bandpass ran from about 4020 to 6775 Å, with a gap of about 75 Å, from 5335 to 5410 Å, due to the physical spacing of the CCD detectors.

The program stars are divided into three groups, i.e., Group I (objects that are known binaries), Group II (objects that are known to be radial velocity variables), and Group III (objects with no information on radial velocity variations). Such a classification helps in comparing the abundance patterns of the Group III objects with their counterparts observed in Group I and Group II objects. In particular, it would be interesting to check if any signature derived from the surface chemical composition of Group III objects can be related to binarity. The latter is an essential requirement to explain the surface chemical composition of CH stars characterized by enhancements of carbon and neutron-capture elements.

2.1. Stellar Atmospheric Parameters and Elemental Abundances

Detailed description of the procedures used for the calculation of the basic atmospheric parameters and elemental abundances, along with the results, are given in Goswami et al. (2006, 2016), Goswami & Aoki (2010), Karinkuzhi & Goswami (2014, 2015). It is important to notice that, to date, our sample is the largest one determined with the same analysis technique and atmosphere models. Here we briefly discuss the procedures that are relevant for the present work. The atmospheric parameters for deriving the chemical abundances are determined using a set of unblended Fe I and Fe II lines. Elemental abundances are derived from measuring the equivalent widths for a few elements whenever we could measure more than one line for that element. We have done spectrum synthesis calculation for the elements that are known to be affected by hyperfine splitting. These calculations are performed by using a recent version of MOOG (Sneden 1973) assuming local thermodynamic equilibrium (LTE). A detailed error calculation for the elemental abundances presented in Tables 1–3 is discussed in the next Section.

2.2. Error Analysis

We have calculated the errors in our abundance results as described in Ryan et al. (1996). The errors in the elemental abundances have contributions from the uncertainty in measurement of the atmospheric parameters and equivalent widths. The errors in the equivalent width also have an effect on the measurement of surface gravity and micro-turbulent velocities. Inaccurate *gf*-values also contribute to the errors in the elemental abundances. For the elements whose abundances have been determined using the spectrum synthesis method, the error is uniformly taken as 0.2 dex. This estimate takes into account the fitting error (0.1 dex) and the error in *gf*-values (0.1 dex). This error evaluation holds for Sc, V, Mn, Ba, La, and Eu. Moreover, we could see a clear variation in the abundance profiles when the synthetic spectra are plotted with ±0.2 dex. For a few objects we have calculated the elemental abundances using a single line. In that case the error is expected to be determined from the measurement of atmospheric parameters only. To find the minimum error for each star, we have considered the respective standard deviation of the iron abundances for each object (approximately 0.1 dex), along with the uncertainties in temperature, micro-turbulent velocities, and surface gravities. We have assumed an error of 100 K in the effective temperature, which leads to an error of 0.1 dex in abundances. Similarly, we estimate 0.03 dex from gravity variations and 0.06 dex from micro-turbulence changes (corresponding to a change of 0.5 km s^{-1}). These values are typically accepted as the minimum error in giants and subgiants (Ryan et al. 1996; Aoki et al. 2007). The total minimum error is calculated using Equation (1) and the value is found to be 0.12. This value is assumed as the error for elements for which a single line is used for the abundance calculation.

$$E_r = \sqrt{E_{r1}{}^2 + E_{r2}{}^2 + E_{r3}{}^2 + E_{r4}{}^2 + E_{r5}{}^2 ..... + E_{rm}{}^2}. \quad (1)$$

When more than one line is used for the abundance calculation, the standard deviation of the abundances derived using individual lines is taken as the error. In Tables 1–3, we present the errors for the elements for which abundances are determined by equivalent width measurements of two or more lines. In Table 4, we have presented the [ls/Fe][4], [hs/Fe][5] and [hs/ls][6] with approximate errors in the calculation. At the end of the table, we have added an object HE 1305+0007, which was analyzed and found to be a CEMP r/s star (Goswami et al. 2006). Errors in [ls/Fe], [hs/Fe] and [hs/ls] are calculated using Equation (1), by taking the respective error for each elements presented in Tables 1–3. For single lines we have used an error equal to 0.12 dex and for the synthesized abundances 0.2 dex. As can be noticed from Equation (1), the error increases in each step, thereby increasing the error in the [hs/ls] index.

3. THEORETICAL MODELS

Theoretical models presented in this paper have been computed with the FUNS (FUll Network Stellar) evolutionary

[4] [ls/Fe] = ([Sr/Fe]+[Y/Fe]+[Zr/Fe])/3.
[5] [hs/Fe] = ([Ba/Fe]+[La/Fe]+[Nd/Fe]+[Ce/Fe]+[Sm/Fe])/5.
[6] [hs/ls] = [hs/Fe]–[ls/Fe].

Table 1
Elemental Abundances: Light Elements C, Na, Mg, Ca, and Ti

Star	[C]	[Na I]	[Mg I]	[Ca I]	[Sc II]	[Ti I]	[Ti II]	References
Group I								
HD 26	7.7	5.35	6.98	6.44 ± 0.11	3.73 ± 0.06	3.96 ± 0.30	⋯	1
HD 5223	7.9	4.57	6.05	4.35	⋯	3.35	⋯	2
[b]HD 16458	8.65	6.17 ± 0.14	6.92 ± 0.04	5.94	2.50	4.56 ± 0.23	4.66 ± 0.28	3
[a]HD 122202	8.26	⋯	7.22	6.01	⋯	⋯	4.63 ± 0.17	4
HD 198269	8.9	4.30	6.03 ± 0.09	4.78 ± 0.14	1.51	3.09 ± 0.14	3.33 ± 0.22	1
HD 201626	8.22	5.19	6.83 ± 0.20	5.57 ± 0.15	1.70	4.25 ± 0.27	4.32 ± 0.25	3
[a]HD 204613	8.64	6.01 ± 0.24	7.40 ± 0.16	6.20 ± 0.18	2.98	4.92 ± 0.24	5.07 ± 0.20	4
HD 209621	7.7	4.10	5.76	4.45	1.92	⋯	3.70	5
[a]HD 216219	8.55	6.32 ± 0.12	7.51 ± 0.20	6.28 ± 0.22	2.70	4.84 ± 0.20	5.02 ± 0.27	3
HD 224959	8.0	3.95	5.50	4.29 ± 0.06	⋯	2.92 ± 0.15	2.97 ± 0.21	5
Group II								
[a]HD 4395	8.09	6.24 ± 0.19	7.49 ± 0.28	6.16 ± 0.22	2.80	4.78 ± 0.22	4.96 ± 0.24	3
[b]HD 55496	7.91	5.08	6.37	5.28	⋯	3.31	3.25	4
[b]HD 48565	8.39	5.76 ± 0.04	7.09 ± 0.23	5.83 ± 0.22	2.35	4.35 ± 0.07	4.61 ± 0.23	3
HD 92545	8.86	5.87 ± 0.03	7.23 ± 0.12	6.05 ± 0.23	⋯	4.72 ± 0.20	5.20 ± 0.24	4
HD 104979	8.16	5.90 ± 0.04	7.34 ± 0.06	6.10 ± 0.24	2.78	4.78 ± 0.16	4.96 ± 0.20	4
HD 107574	8.21	6.01 ± 0.18	⋯	5.85 ± 0.09	2.27	4.57 ± 0.20	4.60	4
Group III								
[b]HD 5395	8.09	5.54 ± 0.14	7.41 ± 0.27	6.09 ± 0.18	2.85	4.74 ± 0.21	4.84 ± 0.25	3
HD 81192	⋯	5.38 ± 0.15	7.32 ± 0.11	5.99 ± 0.19	2.8	4.65 ± 0.20	4.65 ± 0.20	3
HD 89668	8.31	6.12 ± 0.23	7.68	6.81 ± 0.17	2.92	4.51 ± 0.20	4.39 ± 0.22	4
HD 111721	7.36	5.13 ± 0.14	6.88 ± 0.16	5.61 ± 0.21	⋯	4.25 ± 0.24	3.82 ± 0.25	4
HD 125079	8.39	6.33 ± 0.09	7.32 ± 0.27	6.16 ± 0.20	2.89	5.08 ± 0.25	5.17	3
HD 126681	⋯	5.01 ± 0.14	7.07	5.48 ± 0.20	⋯	4.50 ± 0.01	4.60 ± 0.15	4
HD 148897	7.16	4.86 ± 0.14	7.14 ± 0.07	5.48 ± 0.23	1.70	3.99 ± 0.27	4.34 ± 0.20	4
HD 164922	8.47	6.38 ± 0.27	8.12	6.47 ± 0.20	2.81	5.38 ± 0.19	5.18 ± 0.23	4
HD 167768	7.91	5.70 ± 0.25	7.19 ± 0.26	6.02 ± 0.22	2.91	4.56 ± 0.22	3.90 ± 0.28	4
HD 188650	8.09	6.47 ± 0.09	7.34 ± 0.11	5.83 ± 0.20	2.05	2.83 ± 0.10	2.83 ± 0.20	3
HD 214714	8.09	6.29 ± 0.15	7.18 ± 0.21	6.13 ± 0.20	2.16	4.36 ± 0.20	4.89 ± 0.15	3
HE 1152-0355	7.7	⋯	6.25	⋯	⋯	⋯	4.15	2
HE 1305+0007	8.20	4.40	5.75	4.41	1.15	⋯	3.70	2

Notes.
[a] Sub-giant CH stars.
[b] Objects are also included in Ba star catalog of Lu (1991).
References. (1) Goswami et al. (2016), (2) Goswami et al. (2006), (3) Karinkuzhi & Goswami (2014), (4) Karinkuzhi & Goswami (2015), (5) Goswami & Aoki (2010).

code (Straniero et al. 2006, and reference therein). In the last 15 years, main upgrades to the code have been:

1. *Treatment of convective borders*: in FUNS, convective borders are fixed by the Schwarzschild criterion, while the temperature gradient in the convective unstable regions is computed in the framework of the Mixing Length Theory in the formulation by Cox & Giuli (1968). When the H-rich opaque convective envelope penetrates the underlying He-rich radiative region (i.e., during a TDU), a discontinuity arises at the convective/radiative interface. If we perturb such a border, we would find it unstable. In order to overcome this problem, we hypothesize that convective eddies penetrate beyond the formal Schwarzschild border and we mimic it by adding an exponentially decaying profile of velocities at the base of the convective envelope (see Cristallo et al. 2009b, 2011 for its calibration; see also Section 4). Such an algorithm smooths the radiative temperature gradient, thus removing the aforementioned discontinuity.
2. *^{13}C pocket formation*: the introduction of the exponentially decaying profile of convective velocities implies two further consequences: a more efficient TDU and the mixing of a limited amount of protons in the underlying ^{12}C-rich layers. We limit the extension of this extra-mixed zone to two pressure scale heights (2 H_P), starting from the formal Schwarzschild border. When this region heats up, a tiny ^{13}C enriched layer forms. The upper region of the ^{13}C pocket is partially overlapping with a ^{14}N pocket, which acts as a strong neutron poison via the ^{14}N(n, p)^{14}C reaction. The larger the mass of the H-exhausted core, the thinner the ^{13}C pocket. Thus, in low mass models the pockets formed after the first TPs dominate the following s-process nucleosynthesis. As the initial stellar mass increases, the predominance of the ^{13}C $(\alpha, n)^{16}$O neutron source is progressively substituted by ^{22}Ne$(\alpha, n)^{25}$Mg. In fact, the core mass growth implies a reduction of the ^{13}C pocket mass extension and an increase of the maximum temperature attained at the base of the convective shells during TPs. Therefore, the resulting surface s-process distribution strongly depends on the initial stellar mass (see Cristallo et al. 2015b).

Table 2
Elemental Abundances: Light Elements V, Cr, Mn, Co, Ni, and Zn

Star	[V I]	[Cr I]	[Cr II]	[Mn I]	[Co I]	[Ni I]	[Zn I]	References
Group I								
HD 26	⋯	4.34	⋯	4.05	⋯	5.06	3.49	1
HD 5223	⋯	⋯	⋯	⋯	3.70	⋯	⋯	2
[b]HD 16458	3.60	5.28 ± 0.26	⋯	4.80	4.76 ± 0.18	5.73 ± 0.25	4.38 ± 0.20	3
[a]HD 122202	⋯	5.12	⋯	⋯	⋯	5.74 ± 0.16	4.56	4
HD 198269	2.1	3.53 ± 0.18	⋯	3.23 ± 0.16	⋯	4.19 ± 0.14	⋯	1
HD 201626	⋯	3.66 ± 0.25	⋯	⋯	3.53	4.73 ± 0.25	3.17	3
[a]HD 204613	3.75	5.34 ± 0.28	5.48 ± 0.25	4.82	4.49 ± 0.07	6.03	⋯	4
HD 209621	⋯	3.50	⋯	⋯	⋯	4.28	2.90	5
[a]HD 216219	3.70	5.38 ± 0.20	5.59	4.90	4.78 ± 0.25	6.40 ± 0.23	4.59 ± 0.21	3
HD 224959	⋯	2.98 ± 0.16	⋯	⋯	⋯	3.90	⋯	1
Group II								
[a]HD 4395	3.70	5.49 ± 0.29	5.63 ± 0.03	5.00	4.57 ± 0.25	6.05 ± 0.21	4.62	3
[b]HD 55496	2.70	3.80	3.94	⋯	⋯	4.56	3.13	4
[b]HD 48565	3.20	4.86 ± 0.15	4.73 ± 0.02	−0.42	−0.15 ± 0.25	−0.17 ± 0.20	−0.18 ± 0.13	3
HD 92545	⋯	5.28 ± 0.25	⋯	⋯	5.51 ± 0.11	6.03 ± 0.12	⋯	4
HD 104979	3.79	5.36 ± 0.23	5.44 ± 0.24	4.90	4.94 ± 0.13	6.01 ± 0.24	4.31 ± 0.20	4
HD 107574	⋯	5.09 ± 0.25	4.73	⋯	⋯	5.59 ± 0.12	⋯	4
Group III								
[b]HD 5395	3.52	5.21 ± 0.06	5.88	4.65	4.88 ± 0.20	5.90 ± 0.21	4.65	3
HD 81192	3.60	4.81 ± 0.19	4.91 ± 0.19	4.49	4.70 ± 0.08	5.81 ± 0.18	3.98 ± 0.22	3
HD 89668	⋯	5.42 ± 0.23	5.24	5.60	4.56 ± 0.25	5.98 ± 0.23	⋯	4
HD 111721	⋯	4.32 ± 0.20	4.22 ± 0.14	⋯	⋯	5.05 ± 0.22	⋯	4
HD 125079	3.94	5.40 ± 0.25	⋯	4.99	4.77 ± 0.20	6.12 ± 0.24	4.55 ± 0.11	3
HD 126681	⋯	4.84 ± 0.25	⋯	⋯	⋯	5.25 ± 0.23	⋯	4
HD 148897	2.80	4.40 ± 0.20	4.62	3.83	3.94 ± 0.15	5.08 ± 0.20	3.86 ± 0.18	4
HD 164922	4.63	5.91 ± 0.17	5.93 ± 0.03	5.76	5.28 ± 0.25	5.28 ± 0.25	4.98 ± 0.26	4
HD 167768	5.33	5.04 ± 0.20	4.92	4.32	4.38 ± 0.11	5.63 ± 0.27	4.29 ± 0.03	4
HD 188650	3.30	5.14 ± 0.23	5.19	4.69	4.52 ± 0.27	5.61 ± 0.17	4.11 ± 0.04	3
HD 214714	3.21	4.97 ± 0.20	5.06 ± 0.15	4.55	4.51 ± 0.25	5.62 ± 0.17	4.14	3
HE 1152-0355	⋯	⋯	⋯	⋯	⋯	⋯	⋯	2
HE 1305+0007	⋯	⋯	⋯	3.50	⋯	−3.95	⋯	2

Notes.
[a] Sub-giant CH stars.
[b] Objects are also included in Ba star catalog of Lu (1991).
References. (1) Goswami et al. (2016), (2) Goswami et al. (2006), (3) Karinkuzhi & Goswami (2014), (4) Karinkuzhi & Goswami (2015), (5) Goswami & Aoki (2010).

3. *Mass-loss formula*: For the pre-AGB phase we use the classical Reimers mass-loss rate (by setting $\eta = 0.4$), while for the AGB phase we calibrate the mass loss rate on the period–K band luminosity relation proposed by Whitelock et al. (2003), who studied a sample of O-rich and C-rich giant stars in the Magellanic Clouds (see Straniero et al. 2006 for details). We use the same prescription for the whole range of initial stellar masses and metallicities.
4. *C-rich molecular opacities*: depending on the C/O ratio, O-bearing or C-bearing molecules represent the dominant opacity source in the coolest layers of the convective envelope (see e.g., Marigo 2002). Since the carbon reservoir of the envelope increases with the TDU number, the opacity of those layers increases as well, implying more expanded and cooler structures (Cristallo et al. 2007). As a consequence, the use of C-rich molecular opacities leads to a larger mass loss rate with respect to a case in which a solar-scaled distribution is used to calculate opacities.
5. *Rotation*: the effects induced by rotation on the s-process nucleosynthesis are discussed in more detail in Piersanti et al. (2013). Here, we only recall that the combined effect of Eddington–Sweet circulations and Goldreich–Schubert–Fricke instabilities smears off the profiles of the ^{13}C and ^{14}N pockets. As a consequence, the *neutron-to-seed* ratio is lower and, thus, the efficiency of the s-process decreases. Our reference models set is computed without rotation. In Section 5 we present a new set of 1.5 $M_{\odot}$ rotating AGB models at different metallicities.
6. *Nuclear network*: the physical evolution of FUNS models is coupled with a full nuclear network (from hydrogen to lead, at the termination of the s-process path). This allows us to directly follow the s-process nucleosynthesis avoiding post-process calculations. Our network includes about 500 isotopes linked by more than 1000 reactions (Cristallo 2006; Straniero et al. 2006).

Our theoretical models (those previously published and those presented in this paper) are available as a part of the online

Table 3
Elemental Abundances: Heavy Elements

Star	[Sr I]	[Y II]	[Zr II]	[Ba II]	[La II]	[Ce II]	[Pr II]	[Nd II]	[Sm II]	[Eu II]	[Dy II]	References
Group I												
HD 26	3.7	1.95	2.6	2.95	1.51 ± 0.05	2.08 ± 0.13	1.20 ± 0.17	1.75 ± 0.10	1.74 ± 0.30	0.1	⋯	1
HD 5223	2.25	0.80	2.10	1.95	0.85	1.75	⋯	0.95	0.65	⋯	⋯	2
[b]HD 16458	3.64	3.02 ± 0.25	3.11 ± 0.21	2.70	1.90	2.40 ± 0.21	1.88 ± 0.08	2.35 ± 0.17	2.23 ± 0.18	0.53	⋯	3
[a]HD 122202	⋯	3.02	⋯	1.87	1.40	2.57	1.34 ± 0.14	⋯	2.50	⋯	⋯	4
HD 198269	1.95	0.38	1.36 ± 0.06	0.65 ± 0.14	1.19 ± 0.15	0.15 ± 0.09	0.88 ± 0.11	0.84 ± 0.13	⋯	⋯	1	
HD 201626	⋯	⋯	⋯	2.90	1.50	2.08 ± 0.21	1.41	2.30 ± 0.22	1.25 ± 0.25	⋯	0.72	3
[a]HD 204613	4.31	2.94 ± 0.11	3.49 ± 0.04	2.97	2.10	2.58 ± 0.04	1.99	2.23 ± 0.20	2.38 ± 0.17	0.34	2.67	4
HD 209621	2.0	0.65	2.45	1.95	1.62	1.70	0.95	1.40	0.55	−0.05	⋯	5
[a]HD 216219	4.54	3.03 ± 0.22	3.39 ± 0.15	3.13	1.99	2.43	1.67 ± 0.15	2.17 ± 0.25	1.74 ± 0.20	0.41	⋯	3
HD 224959	2.0	0.01	1.82 ± 0.12	1.21 ± 0.05	1.44 ± 0.17	0.64 ± 0.11	1.33 ± 0.09	1.36 ± 0.25	0.09	⋯	1	
Group II												
[a]HD 4395	3.81	2.67 ± 0.21	2.98 ± 0.22	2.77	1.97	1.81 ± 0.25	1.05	2.06 ± 0.17	1.90 ± 0.24	⋯	⋯	3
[b]HD 48565	4.06	2.70 ± 0.13	2.90 ± 0.04	3.10	2.00	2.41 ± 0.17	1.10 ± 0.02	2.37 ± 0.05	1.60 ± 0.02	0.22	⋯	3
[b]HD 55496	2.35	1.65 ± 0.19	1.70	1.33	⋯	0.30	0.27	⋯	⋯	⋯	⋯	4
HD 92545	⋯	0.23 ± 0.21	⋯	0.91	0.95	1.6	⋯	⋯	⋯	⋯	⋯	4
HD 104979	3.60	2.61 ± 0.23	3.13	2.80	1.93	2.33 ± 0.25	1.44 ± 0.20	2.25 ± 0.25	2.05 ± 0.24	0.61	⋯	4
HD 107574	⋯	2.57 ± 0.19	⋯	2.48	1.51	1.52	⋯	⋯	⋯	⋯	⋯	4
Group III												
[b]HD 5395	2.94	2.02 ± 0.11	⋯	1.96	1.13	1.40 ± 0.17	1.26 ± 0.20	1.95 ± 0.12	⋯	0.62	2.28	3
HD 81192	2.99	1.80 ± 0.11	2.20 ± 0.12	1.79	0.90	0.92 ± 0.11	⋯	2.00 ± 0.16	1.35 ± 0.25	⋯	1.84	3
HD 89668	3.79	2.57 ± 0.30	⋯	1.74	2.78	2.91	2.18	2.65 ± 0.20	2.05	0.71	⋯	4
HD 111721	⋯	1.15 ± 0.21	⋯	0.97	0.33	2.07 ± 0.09	⋯	2.44 ± 0.14	⋯	⋯	⋯	4
[a]HD 125079	4.33	3.08 ± 0.17	⋯	3.05	⋯	2.41 ± 0.27	1.53	2.46 ± 0.14	1.39	⋯	⋯	
HD 126681	⋯	1.31 ± 0.06	⋯	1.52	⋯	1.25	⋯	1.73 ± 0.10	1.16	⋯	⋯	4
HD 148897	2.24	1.25 ± 0.17	1.13	0.53	0.43	0.43 ± 0.21	⋯	0.59 ± 0.21	0.60 ± 0.20	⋯	0.17	4
HD 164922	3.94	2.58 ± 0.30	⋯	2.68	1.51	1.72 ± 0.15	⋯	⋯	⋯	⋯	⋯	4
HD 167768	3.13	2.21 ± 0.24	2.23 ± 0.02	1.25	0.03	1.08 ± 0.30	⋯	1.55 ± 0.22	1.35 ± 0.24	0.22	1.62	4
HD 188650	⋯	1.71 ± 0.16	⋯	1.69	⋯	1.08 ± 0.17	0.81	1.37	0.42 ± 0.14	⋯	⋯	3
HD 214714	⋯	2.08 ± 0.20	1.96 ± 0.27	1.51	⋯	1.28 ± 0.17	1.29 ± 0.28	1.46 ± 0.24	1.20 ± 0.16	⋯	⋯	3
HD 1152-0355	⋯	1.05	1.32	2.45	1.40	⋯	⋯	0.58	0.58	⋯	⋯	2
HE 1305+0007	1.75	0.95	2.65	2.50	1.70	2.12	1.10	2.05	1.62	0.50	⋯	2

Notes.
[a] Sub-giant CH stars.
[b] Objects are also included in Ba star catalog of Lu (1991).
References. (1) Goswami et al. (2016), (2) Goswami et al. (2006), (3) Karinkuzhi & Goswami (2014), (4) Karinkuzhi & Goswami (2015), (5) Goswami & Aoki (2010).

Table 4
Errors in [ls/Fe] and [hs/Fe]

Star	[Fe/H]	[ls/Fe]	[hs/Fe]	[hs/ls]
Group I				
HD 26	−1.11	1.31 ± 0.34	1.69 ± 0.44	0.38 (⩽±0.50)
HD 5223	−2.06	1.19 ± 0.28	1.78	0.59 (⩽±0.39
HD 16458	−0.65	1.34 ± 0.30	1.50 ± 0.45	0.16 (⩽±0.45)
HD 122202	−0.63	1.44 ± 0.20	1.16 ± 0.28	−0.28 (⩽±0.28)
HD 198269	−2.03	0.64 ± 0.28	1.55 ± 0.33	0.91 (⩽±0.44)
HD 201626	−1.39	…	1.93 ± 0.45	…
HD 204613	−0.24	1.27 ± 0.23	1.16 ± 0.42	−0.11 (⩽±0.42)
HD 209621	−1.94	0.79 ± 0.28	1.89 ± 0.28	1.1 (⩽±0.45)
HD 216219	−0.17	1.26 ± 0.33	1.01 ± 0.34	−0.25 (⩽±0.34)
HD 224959	−2.42	0.86 ± 0.28	2.24 ± 0.34	1.38 (⩽±0.45)
Group II				
HD 4395	−0.18	0.77 ± 0.20	0.82 ± 0.20	0.05 (⩽±0.20)
HD 48565	−0.59	1.24 ± 0.31	1.47 ± 0.42	0.23 (⩽±0.42)
HD 55496	−1.49	0.73 ± 0.27	0.38 ± 0.41	−0.35 (⩽±0.41)
HD 92545	−0.21	0.23 ± 0.29	1.15 ± 0.20	0.92 (⩽±0.29)
HD 104979	−0.26	0.85 ± 0.30	1.03 ± 0.51	0.18 (⩽±0.51)
HD 107574	−0.48	1.02 ± 0.27	0.87 ± 0.29	−0.15 (⩽±0.29)
Group III				
HD 5395	−0.24	0.16 ± 0.22	0.27 ± 0.44	0.11 (⩽±0.44)
HD 81192	−0.50	0.26 ± 0.21	0.34 ± 0.27	0.08 (⩽±0.27)
HD 89668	−0.13	0.81 ± 0.48	1.16 ± 0.32	0.35 (⩽±0.48)
HD 111721	−1.11	0.05 ± 0.29	0.98 ± 0.20	0.93 (⩽±0.29)
HD 125079	−0.18	1.32 ± 0.23	0.93 ± 0.25	−0.39 (⩽±0.25)
HD 126681	−0.90	0.02 ± 0.20	0.80 ± 0.34	0.78 (⩽±0.34)
HD 148897	−1.02	−0.13 ± 0.28	0.01 ± 0.39	0.14 (⩽±0.39)
HD 164922	0.22	0.47 ± 0.36	0.10 ± 0.38	−0.37 (⩽±0.38)
HD 167768	−0.51	0.51 ± 0.31	0.14 ± 0.42	−0.37 (⩽±0.42)
HD 188650	−0.45	−0.03 ± 0.20	0.23 ± 0.20	0.26 (⩽±0.20)
HD 214714	−0.35	−0.03 ± 0.21	0.14 ± 0.43	0.17 (⩽±0.43)
HE 1152-0355	−1.27	0.07 ± 0.28	1.11 ± 0.28	1.04 (⩽±0.39)
HE 1305+0007	−2.0	1.11 ± 0.28	2.52 ± 0.28	1.30 (⩽±0.39)

Note. The errors given in the 5th column in parentheses are the upper limits of errors in [ls/Fe] and [hs/Fe].

FRUITY (FUNS Repository of Updated Isotopic Tables & Yields) database[7] (Cristallo et al. 2011, 2015b). From this web platform it is possible to freely download the chemical (elemental and isotopic surface distributions, yields, s-process indexes, etc.) as well as the physical features of the models (masses, luminosities, gravities, number of Thermal Pulses and TDUs, TDU efficiency, etc.).

4. COMPARISON BETWEEN OBSERVATIONS AND FRUITY MODELS

In Figure 1 we report the [hs/ls] ratios of our CH sample (see Table 4) as a function of the iron content [Fe/H]. We plot the three groups with different symbols: circles (Group I), squares (Group II), and triangles (Group III). According to this plot, the groups seem to represent a homogeneous sample. We focus on the [hs/ls] s-process index because our low mass models attain a nearly asymptotic value after a few TDUs. Therefore, our [hs/ls] ratios are almost independent from the adopted mass-loss rate (see the discussion in Cristallo et al. 2011), thus reducing the degeneracy in the free parameter space. The theoretical behavior of the models is clear: starting from the highest computed metallicity, there is an increase of the [hs/ls] value down to [Fe/H] ∼ −0.7. This is due to the fact that, at large metallicities, mostly ls elements are synthesized, while with decreasing Z the *neutron-to-seed* ratio increases and the hs component is produced too. At lower [Fe/H], lead starts being produced, basically freezing the [hs/ls] ratio to a value of about 0.5–0.6. Apart from the 4 $M_{\odot}$ star, in which the ^{22}Ne$(\alpha, n)^{25}$Mg contribution dominates, the other models present quite similar [hs/ls] ratios for a fixed metallicity. Observations show a different trend. Apart from a couple of isolated stars, two distinct features appear: an increasing [hs/ls] ratio down to very low metallicities and a definitely larger spread for a fixed [Fe/H]. A further criticality may arise when comparing the theoretical [ls/Fe] and [hs/Fe] to observations (see Figure 2). As already stressed before, CH stars owe their s-process surface enrichment to a transfer episode from the already extinct AGB companion. Many of our CH stars are in fact confirmed binaries (those belonging to Group I) and others have known radial velocity variations (those belonging to Group II). Furthermore, when comparing theoretical models to observation, a possible dilution due to the evolutionary status of the accreted star may be taken into account (see e.g., Bisterzo et al. 2011), as well as long-lasting processes, such as gravitational settling (see e.g., Stancliffe 2010). It is far from the purpose of this paper to determine the binary system properties of our CH sample.

[7] http://www.oa-teramo.inaf.it/fruity

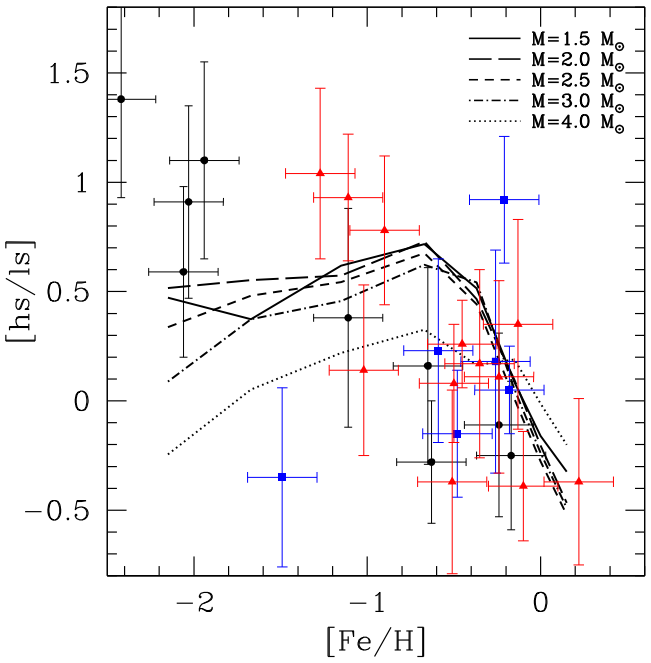

Figure 1. [hs/ls] ratios of our CH sample as a function of the metallicity compared to FRUITY models. Symbols refer to the three groups identified in Table 4: circles (Group I), squares (Group II), and triangles (Group III).

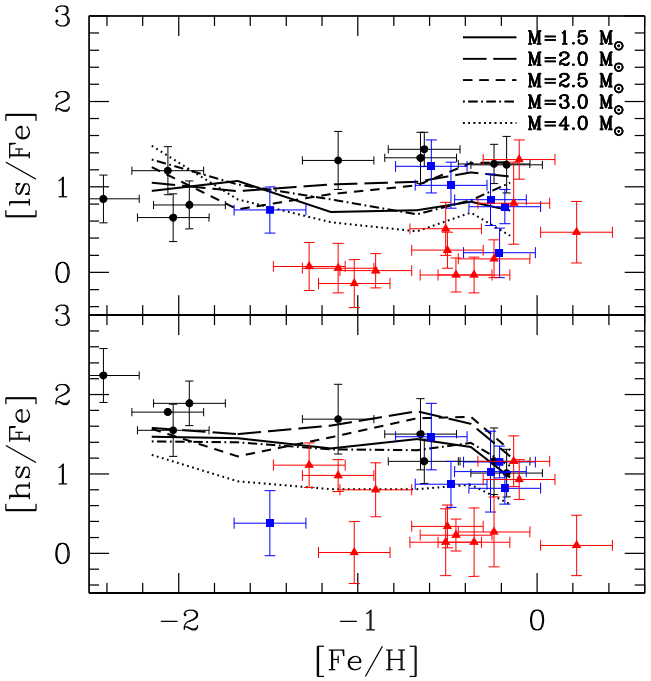

Figure 2. As in Figure 1, but for [ls/Fe] and [hs/Fe] (upper and lower panel, respectively).

However, we can provide some general considerations based on first principles. The degree of the dilution depends on the evolutionary phase of the observed CH star. Depending on the initial mass, these objects may have no convective envelope during the main sequence phase: in this case, no dilution has to be explicitly taken into account. The situation is different if the envelope is penetrating downward while ascending the Red-Giant Branch (sub-giant stars) or if it is already receding (red-giant stars). In the second case, FDU has already mixed the whole envelope and the dilution factor definitely grows (up to 1 dex). FRUITY models with initial mass $M \sim (2.0–2.5)\ M_{\odot}$ show large enough final surface s-process enhancements to account for the majority of the observed stars. However, our models may underestimate the s-process overabundances in case of a large dilution. It is worth noticing that, according to Figure 2, a non-negligible fraction of CH stars belonging to Group III (triangles) shows no absolute surface s-process enhancement (within the errors). Therefore, some of these objects may not be CH stars, although they are included in the catalog of Bartkevicius (1996).

5. THE EFFECTS OF ROTATION

In Section 3 we briefly mentioned the effects that rotation has on the s-process nucleosynthesis. Piersanti et al. (2013) demonstrated that the mixing induced by rotation (mainly Eddington–Sweet circulations and Goldreich–Schubert–Fricke instabilities) leads to a decreasing *neutron-to-seed* ratio with increasing initial rotation velocity ($v_{\rm ini}^{\rm rot}$). For a fixed initial mass and metallicity, the larger $v_{\rm ini}^{\rm rot}$, the lower the [hs/ls] and the [Pb/hs] ratios. This is evident in Figure 4, where we compare the reference 1.5 $M_{\odot}$ models FRUITY set (labelled REF) to an analogous set of rotating models with $v_{\rm ini}^{\rm rot} = 60\ {\rm km\ s^{-1}}$ (labelled V60). Major effects occur at [Fe/H] ~ -0.8, showing an [hs/ls] difference larger than a factor of 10. At low metallicities, such a difference is less evident because, in this case, lead is the most affected s-process element (see Figure 9 of Piersanti et al. 2013). Unfortunately, lead could not be detected in the majority of the spectra in our sample, otherwise it would be the ideal indicator to verify the presence of rotation in the donor AGB stars.

Depending on the environmental formation process, a star could approach the main sequence with different initial rotation velocities. In principle, the larger the mass is, the larger the expected rotation velocity is. Moreover, the lower the metallicity is, the higher the initial rotation velocity is (because objects are more compact). As a consequence, the effect of rotation of the ongoing nucleosynthesis may differ from star to star. It is therefore reasonable to hypothesize that a spread in $v_{\rm ini}^{\rm rot}$ leads to a spread in the s-process efficiency. However, independently from $v_{\rm ini}^{\rm rot}$, the [ls/Fe] and [hs/Fe] indexes of rotating models are lower than the corresponding non-rotating cases (see lower panel of Figure 4). This implies that a large fraction of CH stars cannot be fitted by our rotating AGB models, even taking into account the possibility that a larger AGB mass polluted the observed accreted CH star. In summary, the introduction of rotation alone improves the fit to the observed [hs/ls] ratios, but absolute surface s-process values pose severe limitations to the initial rotational velocity. It is worth remembering that recent asteroseismologic measurements (see e.g., Mosser et al. 2012) suggest that the cores of red clump stars (thus in an evolutionary phase prior to the AGB) have a lower rotation velocity than what we find in our models. Therefore, the inclusion of some form of angular momentum re-distribution (Marques et al. 2013) or braking (Spruit 2002) is necessary. Among the possible scenarios to slow down stellar cores, magnetic fields are the most promising candidates. Note, we also call to mind that low metallicity stars are more compact than their solar-metallicity counterparts and, therefore, they are expected to rotate faster for a fixed initial angular momentum. These considerations have to be taken into account when assigning the initial $v_{\rm ini}^{\rm rot}$ to a model. Notwithstanding, our goal is to highlight general trends rather than giving a quantitative

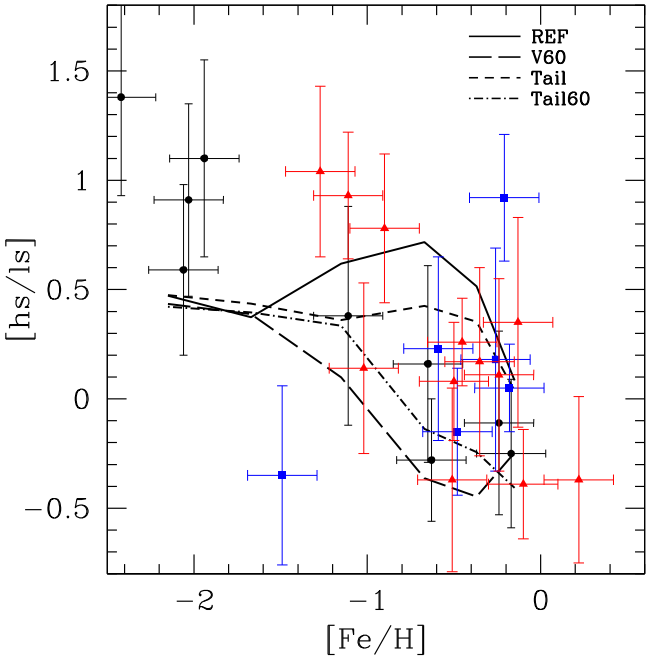

Figure 3. [hs/ls] ratios as a function of the metallicity for a set of 1.5 $M_{\odot}$ stars and different prescriptions for the physics. Various curves refer to: FRUITY models (REF), rotating models with $v_{\rm ini}^{\rm rot} = 60$ km s^{-1} (V60), non-rotating models with extended ^{13}C pockets (Tail), rotating models with $v_{\rm ini}^{\rm rot} = 60$ km s^{-1}, and extended ^{13}C pockets (Tail60). Observations have the same symbols as in Figure 1.

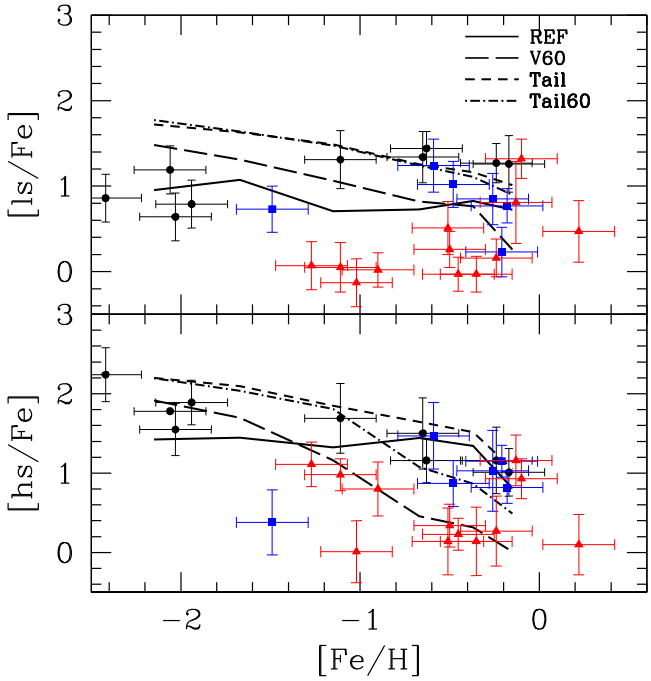

Figure 4. As in Figure 3, but for [ls/Fe] and [hs/Fe] (upper and lower panel, respectively).

picture of the problem. For this reason we limit our analysis to just one mass and one rotation velocity.

6. THE EFFECTS OF A DIFFERENT TREATMENT OF THE RADIATIVE/CONVECTIVE INTERFACES IN AGBS

In Section 3 we already explained in detail our prescription for the handling of the convective/radiative interface at the inner border of the convective envelope. In Cristallo et al. (2011) we discussed the effects of changing the free parameter characterizing our exponential velocity profile and we justified our choice. Recently, we also studied the effects of relaxing the 2 H_P condition we impose at the lower boundary of the extra-mixed zone (Cristallo et al. 2015a). In that paper we let the velocity profile extend down to a layer characterized by a mixing velocity equal to 10^{-11} times the convective velocity at the Schwarzschild border (models labelled "Tail" in Figures 3 and 4). As a net effect, the ^{13}C pockets forming after each TDU present a more extended tail with low ^{13}C abundances and negligible ^{14}N abundances. The need for this kind of extended ^{13}C pockets has been suggested by the comparison of theoretical models with open cluster observations (D'Orazi et al. 2009; Maiorca et al. 2011, 2012) and, more recently, laboratory measurements of isotopic ratios in pre-solar SiC grains (Liu et al. 2014a, 2014b, 2015). The formation of ^{13}C pockets with extended tails leads, in our models, to increased surface s-process overabundances. The differences to the reference FRUITY set slightly increase with decreasing initial iron content (see Figure 4; see also Figure 7 of Cristallo et al. 2015a). The variation in the [hs/ls] ratio is limited, reaching a maximum difference of about 0.3 dex around [Fe/H] ~ -0.8. In summary, the *Tail* models show increased surface final s-process overabundances without largely modifying the [hs/ls] index.

6.1. Extended Undershooting and Rotation

In Figures 3 and 4 we present the 1.5 $M_{\odot}$ set computed with extended ^{13}C pockets and initial rotation velocity $v_{\rm ini}^{\rm rot} = 60$ km s^{-1} (labelled as *Tail60*). The [hs/ls] ratios of the *Tail60* set are slightly larger than those obtained in the *V60* set. Therefore, the possibility to reproduce the observed spread by assuming different rotation velocities is preserved. Notwithstanding, the disagreement between theory and observations still exists at [Fe/H] < -1. The [ls/Fe] indexes are very similar to the *Tail* case, while the [hs/Fe] distribution shows a decrease at large metallicities. This effects could be compensated by an increase of the AGB donor mass (up to 2.5–3.0 $M_{\odot}$), which would provide a large enough s-process pollution to reproduce the most enriched CH stars. In summary, the *Tail60* set seem to provide a satisfactory solution for both the absolute and relative s-process abundances, at least for [Fe/H] > -1. At low metallicities, instead, it clearly emerges that the hs production obtained in our models is not large enough to fit observations.

7. THE CEMP CASE

CH stars discussed in the previous sections belong to a larger class of objects, i.e., stars enriched by mass-transfer from an extinct AGB donor. Historically, these objects have been classified based on their spectrum, quite often coinciding with a metallicity segregation. At large metallicities, Ba-stars are observed, while the equivalents of CH stars at low metallicity are CEMP stars.

CEMP stars represent a significant fraction of the low end of the galactic halo metallicity distribution. Beers & Christlieb (2005) have classified these objects into four major groups based on their heavy element abundance patterns. The most numerous is the CEMP-s group, that exhibits enhancement of slow neutron-capture elements in their surface chemical composition. CEMP stars that are characterized by the

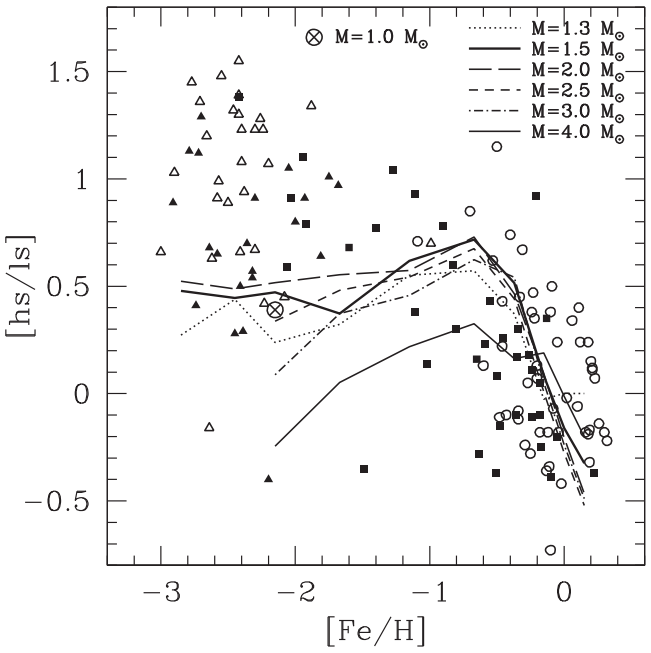

Figure 5. Theoretical [hs/ls] as a function of the metallicity for different masses. Theoretical curves refer to the non-rotating reference FRUITY models. Various symbols refer to: Ba stars (Allen & Barbuy 2006; Smiljanic et al. 2007; Liu et al. 2009; Pereira et al. 2011; Lebzelter et al. 2013; *open circles*); CH stars (Smith et al. 1993; Začs et al. 2000; Goswami et al. 2006; Pereira & Drake 2009; Goswami & Aoki 2010; Pereira & Drake 2011; Liu et al. 2012; Pereira et al. 2012; Karinkuzhi & Goswami 2014, 2015; Goswami et al. 2016; *filled squares*); CEMP-s stars (Preston & Sneden 2001; Aoki et al. 2002a, 2002b; Lucatello 2004; Cohen et al. 2006, 2013; Placco et al. 2013; Roederer et al. 2014; *filled triangles*); CEMP-rs stars (Aoki et al. 2002c; Van Eck et al. 2003; Johnson & Bolte 2004; Lucatello 2004; Barbuy et al. 2005; Ivans et al. 2005; Cohen et al. 2006; Jonsell et al. 2006; Roederer et al. 2008, 2010, 2014; Thompson et al. 2008; Behara et al. 2010; Masseron et al. 2010; Cohen et al. 2013; Cui et al. 2013; Placco et al. 2013; Hollek et al. 2015; Jorissen et al. 2016a; *open triangles*).

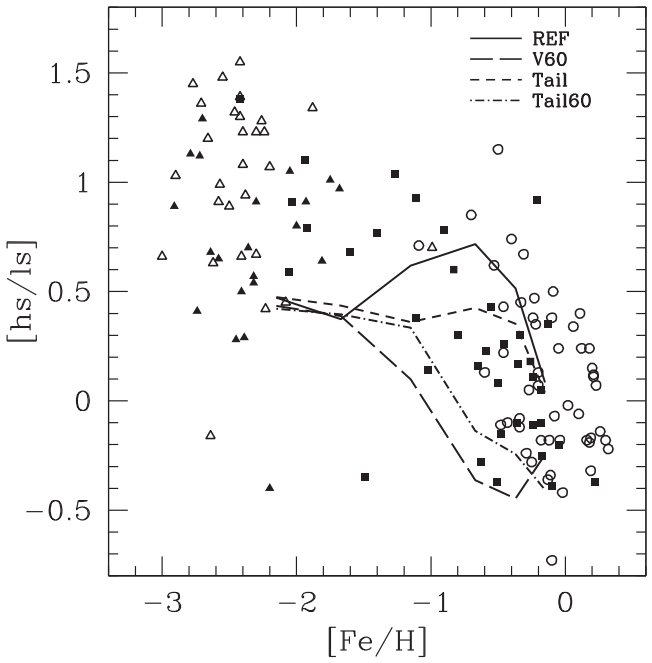

Figure 6. As Figure 5, but for different physics prescriptions.

enhancement of r-process elements are called CEMP-r stars, although this class has very few confirmed examples so far. Another class of CEMP stars exhibits large overabundances of elements produced by both s-process and r-process (the so-called CEMP-rs stars). CEMP stars that do not show enhancement of heavy elements form another class (called CEMP-no stars). We note that, recently Jorissen et al. (2016b) demonstrated that CH and CEMP-s stars lie in the same region of the period–eccentricity diagram and present similar mass-function distributions. Therefore, they suggested that these two classes of objects should be treated as a unique stellar family, as we did in the combined analysis presented in this paper.

It should be noted that not all CEMP-s stars are binaries. In fact, Hansen et al. (2016) densities have recently shown from long term radial velocity monitoring that the binary frequency of CEMP-s stars is about 82 ± 10%. Out of 22 objects that they have studied, 18 of them exhibit clear orbital motion, while four stars appear to be single. Thus they confirmed that the binary frequency of CEMP-s stars is much higher than for normal metal-poor giants, but not 100% as previously claimed. We exclude from our analysis CEMP stars without a clear detection of europium (an r-process element) in order to avoid a wrong identification as CEMP-s or CEMP-rs stars.

In Figure 5 we report our theoretical [hs/ls] ratios for different initial masses and compare them to observations (see the caption for the references). In order to span over a larger metallicity grid, we computed additional low mass models (1.3–1.5–2.0) with [Fe/H] = −2.45 and [Fe/H] = −2.85 (both with [α/Fe] = 0.5). Our set does not reproduce the high [hs/ls] ratios detected in low metallicity CH and CEMP-s stars ([hs/ls] ∼ 1). The same conclusion still holds when adopting different prescriptions for convection and/or rotation (see Figure 6). Note that an increase of the initial stellar mass would not improve the situation. In fact, models with $M \geqslant 2.5\ M_{\odot}$ at low metallicities have quite large core masses at the beginning of the AGB phase and therefore show chemical signatures typical of intermediate mass models at large metallicities (see, e.g., Cristallo et al. 2011). Notwithstanding, we compute additional 2 $M_{\odot}$ models with [Fe/H] = −2.45 with rotation and/or extended tail. With respect to the 1.5 $M_{\odot}$ models, we find increased s-process surface enhancements, but almost the same [hs/ls]. Alternative solutions need thus to be found, as, for example, the introduction of mixing induced by magnetic fields (see Trippella et al. 2016 and references therein). We will test such a possibility in a forthcoming paper.

Useful hints on the needed ^{13}C pocket shape can be derived from theoretical post-processing calculations with constant ad hoc ^{13}C pockets (Bisterzo et al. 2010, 2011, 2012). Those works demonstrated that at low metallicities [hs/ls] ∼ 1 can be obtained and that a good fit to a large number of s-process enriched CEMP stars can be found. In those calculations the ^{13}C pockets are artificially added after each TDU (with a constant mass extension) and the ^{13}C abundance is freely varied within the pockets (Gallino et al. 1998). Within that framework, fits to observations are obtained with ^{13}C pockets characterized by very low ^{13}C abundances (see Figure 17 of Bisterzo et al. 2011).

As already mentioned before, there is a class of CEMP stars showing surface enrichment of elements ascribed to both the s-process and the r-process (the so-called CEMP-rs stars). Those objects show the largest observed [hs/ls] ratios (see asterisks in Figure 5). Actually, there is no consensus on their pollution history (see Abate et al. 2016 and references therein). Among the proposed theories, there is the so-called i-process

(Cowan & Rose 1977), i.e., a nucleosynthetic process providing neutron densities intermediate between those characterizing the s-process ($n_n \sim 10^7\,\mathrm{cm}^{-3}$) and the r-process ($n_n > 10^{21}\,\mathrm{cm}^{-3}$). This range of neutron densities can be attained in low mass low metallicity stars, when protons from the envelope are ingested into the underlying convective He intershell. We refer to this episode as the proton ingestion episode (PIE). The occurrence of such a mixing phenomenon depends on the initial stellar mass and metallicity: the lower the mass and the metallicity, the higher the probability for a PIE to occur. At extremely low metallicities ([Fe/H] < -3), a PIE can be found during the off-center He-burning flash, while for larger Z ($-3 <$ [Fe/H] < -2) it may occur at the first fully developed TP (Hollowell et al. 1990; Fujimoto et al. 2000; Iwamoto et al. 2004; Campbell & Lattanzio 2008; Lau et al. 2009). 3D hydrodynamical simulations confirm this peculiarity, which characterizes very metal-poor models (Woodward et al. 2008). In 2009, we presented the evolution and nucleosynthesis of a 1.5 $M_\odot$ model with [Fe/H] $= -2.45$ and no α enrichment (Cristallo et al. 2009a). That model experiences a strong PIE, with important consequences for the physical and chemical evolution of the structure. In particular, we found that soon after the occurrence of a PIE, a very deep TDU occurs, which carries to the surface the freshly synthesized ^{13}C, ^{14}N, and light s-process elements. Those nuclei are the result of a convective high-temperature H-burning. Since the CNO burning occurs in non-equilibrium conditions, a huge amount of ^{13}C is produced. This leads to a very efficient neutron production from the ^{13}C$(\alpha, \mathrm{n})^{16}$O reaction, with neutron densities reaching $n_n \sim 10^{15}\,\mathrm{cm}^{-3}$. However, the local energy release from in-flight proton burning leads to the splitting of the convective He-shell and stops any further growth of the neutron density. It is important to note that the mass and temporal coordinates of such a splitting strongly depend on the adopted nuclear network. In fact, the split occurs when the energy released by proton capture reactions overwhelms the energy production at the base of the convective shell (see Figure 3 of Cristallo et al. 2009a). The energy budget triggering the convective shell comes from 3α reactions, whose Q value is about 7 MeV. However, when enough ^{13}C has been mixed within the shell, the ^{13}C$(\alpha, \mathrm{n})^{16}$O reaction ($Q \sim 2$ MeV) and the following neutron capture (on average $Q \sim 5$ MeV) provide an additional important energetic contribution. This comes from the fact that, even if the ^{13}C abundance is definitely lower, its α capture cross section is at least 7 orders of magnitude larger than that characterizing the 3α process. Therefore, in order to properly calculate the energetics of PIEs, it is mandatory to use a complete neutron capture network coupled to the physical evolution of the stellar structure. In the 2009 model, we found a very low [hs/ls] ratio after the deep TDU following a PIE. Later, the following standard TDU episodes re-establish the trend expected at low Z, i.e., with the hs component exceeding the ls one. Thus, depending on the initial mass (and, consequently, on the TDU number), the PIE signature can be masked by the following standard s-process nucleosynthesis. A way to trace it, however, exists and it is connected to barium isotopic ratios. The occurrence PIEs, in fact, pushes the nucleosynthesis path far from the β stability valley. Very neutron-rich isotopes are produced, such as ^{135}I (an isotope having a magic number of neutrons, $N = 82$). This radioactive isotope decays to ^{135}Cs and, later, to its stable isobar ^{135}Ba. Therefore, the occurrence of a PIE could be proven by the detection of a very large ^{135}Ba abundance. Note that the cross section of ^{135}I is very low compared to other magic nuclei. Moreover, it has been determined only theoretically. A change in its cross section could determine large variations in the expected surface barium abundance and, thus, its determination should deserve renewed efforts.

The low metallicity models we compute for this paper present a major difference with respect to that presented in Cristallo et al. (2009a), because we add an initial α-elements enhancement ([α/Fe] $= 0.5$). Such an enrichment of α elements, which is normally observed in halo stars (Abia & Rebolo 1989), has strong consequences on the occurrence of PIEs. In fact, the increased initial oxygen abundance makes the H-shell more efficient, thus contrasting the occurrence of the PIE episode itself. As a matter of fact, the only models experiencing PIEs are the 1.3 $M_\odot$ and, to a lesser extent, the 1.5 $M_\odot$ with [Fe/H] $= -2.85$. This is evident in Figure 5, in which the 1.3 $M_\odot$ curve shows a clear decrease at the smallest metallicity, thus confirming that, in our models, the occurrence of PIEs leads to a low [hs/ls]. We verify what happens at larger metallicities ([Fe/H] $= -2.15$) and we find that a very mild PIE occurs in the 1 $M_\odot$ only (crossed dot in Figure 5), without a clear nucleosynthetic signature in the envelope of this model. Thus, the introduction of an initial α enhancement strongly reduces the number of expected stars experiencing PIEs and, consequently, weakens the related scenario for the formation of CEMP-rs stars from low mass, low metallicity AGB stars (see e.g., Abate et al. 2016). Another important issue related to PIEs concerns the use of 1D hydrostatic codes, which necessarily implies a parametric and space-averaged treatment of convection. Recent 3D calculations (Herwig et al. 2011, 2014; Woodward et al. 2015), although computed for a different class of stars (Sakurai objects), confirm the occurrence of the splitting of the convective He-shell, even if with a temporal delay with respect to 1D hydrostatic models. In those models, convective mixing is usually modeled as a pure diffusive process. In our models, we use a time-dependent mixing scheme derived from an algorithm originally proposed by Sparks & Endal (1980) and subsequently modified by Chieffi et al. (1998) and Straniero et al. (2006). Moreover, in order to handle in-flight proton burning, we limit the model temporal step to a fraction (we assume 1/3) of the CNO burning timescale. As a consequence, the splitting occurs after about 0.65 year from the starting of the PIE, later than in the models with diffusive mixing. During that temporal interval, the ^{13}C (which is mixed down to the bottom of the convective shell) accumulates enough to generate a substantial s-process nucleosynthesis. In Figure 7 we report the temporal evolution of the maximum neutron density we obtain in our 1.3 $M_\odot$ model with [Fe/H] $= -2.85$ (upper panel). We attain a very high neutron density for a very short period, because the increase in n_n is interrupted by the splitting of the convective He-shell. The red dot in Figure 7 corresponds to the moment immediately before the splitting of the shell. At that time, the [La/Y] (representative of the [hs/ls] s-process index) within the convective shell is already larger than 2 (see red curve in the lower panel). After the splitting, it still grows almost up to 3 in the lower shell (blue dotted curve), due to the ^{13}C reservoir stored before the splitting. Later, considering the paucity of iron seeds, lead starts being produced at the expense of La (green short-dashed curve). Finally, after about 17 years from

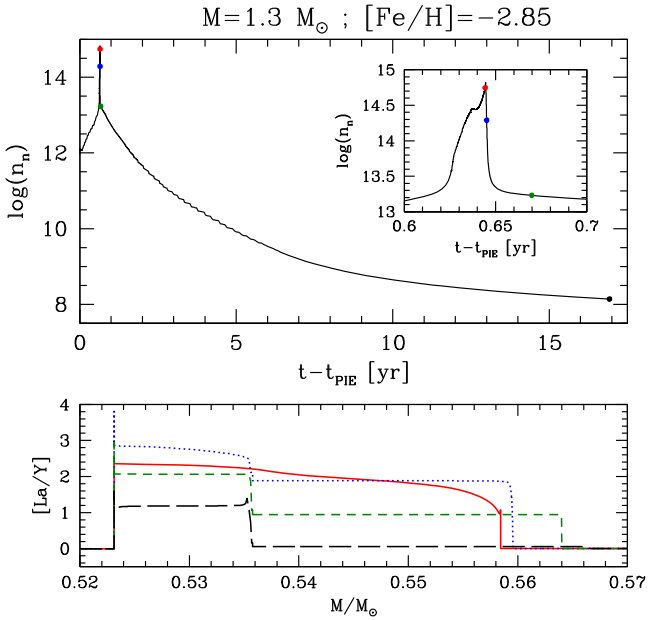

Figure 7. Upper panel: maximum neutron density reached during the PIE of a 1.3 $M_{\odot}$ model with [Fe/H] $= -2.85$ as a function of time from the onset of the PIE. Lower panel: s-process indexes in stellar layers affected by the PIE. Each color refers to a different delay from the onset of the PIE (see corresponding dots in the upper panel). See text for details.

the onset of the PIE, a low [La/Y] value characterizes the lower shell (long-dashed dark curve), while in the upper shell an almost solar value is found. In summary, during a PIE there are layers in which a very large [hs/ls] can be attained, but the following evolution may remove every trace of it. Recently, Dardelet et al. (2015) and Hampel et al. (2016) compared the results of one-zone network calculations to observed CEMP-rs stars. They showed that observed [hs/ls] ratios can be matched with very high neutron densities ($n_n > 10^{15}$ cm^{-3}) lasting for about 0.1 year. Those calculations are very instructive because they identify the characteristics of the process able to reproduce observations. The results they obtain are not so different from what we showed in Figure 7 soon after the occurrence of the splitting of the convective shell. However, post-processing calculations do not include the physical drawback stimulated by a PIE and, therefore, they may miss an important part of the following physical evolution. On the other side, the parametric treatment of PIEs in our 1D stellar evolutionary code may lead to wrong conclusions and the splitting may occur under very different physical conditions, with important consequences on the following evolution.

8. CONCLUSIONS

In this paper we used a homogeneous sample of CH stars observations to constrain AGB models. The homogeneity of such a sample is fundamental in order to exclude discrepancies due to the use of different analysis techniques and/or atmosphere models. We mainly concentrate on the s-process index [hs/ls] (i.e., the ratio between elements belonging to the first and to the second peak of the s-process) because this quantity is almost independent of the number of experienced TDUs. On average, observations show an increasing [hs/ls] with decreasing initial metal content as well as a consistent spread for a fixed metallicity. Theoretical models described here have been calculated with the FUNS code and are available on the web pages of the FRUITY database. We find that our standard set reproduces the increase in the [hs/ls] down to [Fe/H] $= -1$ fairly well. However, when taking into consideration the expected dilution due to the binary origin of CH stars, models are not able to cover the whole observational sample. Such a disagreement can be improved by adopting a different criterion for handling the radiative/convective interface at the base of the convective envelope as well as taking explicitly into consideration the effects induced by rotation. Notwithstanding, even when including the aforementioned physical processes in our stellar evolutionary code, we cannot match the high [hs/ls] ratios observed in low metallicity CH and CEMP stars. We plan to evaluate the effects induced by other physical mechanisms on the ongoing s-process nucleosynthesis, such as mixing induced by magnetic fields. Finally, we check the possibility that PIEs occurring at the beginning of the AGB phase of low mass stars could solve the problem. In our models, even if a PIE episode leads to a provisional and very high local [hs/ls] ratio, the following evolution removes any trace of it and, thus, the surface is characterized by a low [hs/ls] ratio. Moreover, the use of an initial mixture that is enriched in α-elements limits the occurrence of PIEs to low mass models ($M \leqslant 1.3\ M_{\odot}$) at very low metallicities ([Fe/H] $\leqslant -2.85$).

We thank the anonymous referee for valuable comments on the paper. S.C., L.P., and D.G. acknowledge funding from Italian grant PRIN-MIUR 2012 "Nucleosynthesis in AGB stars: An integrated approach" project (20128PCN59). A.G. gratefully acknowledges funding from the DST project SB/S2/HEP-010/2013. We are indebted to M. Quintini for his precious help in managing and updating the FRUITY database web platform. We acknowledge M. Eichler for a careful reading of the manuscript. S.C. thanks S. W. Campbell for stimulating scientific discussions which influenced this paper.

REFERENCES

Abate, C., Stancliffe, R. J., & Liu, Z.-W. 2016, A&A, 587, A50
Abia, C., & Rebolo, R. 1989, ApJ, 347, 186
Allen, D. M., & Barbuy, B. 2006, A&A, 454, 895
Aoki, W., Ando, H., Honda, S., et al. 2002a, PASJ, 54, 427
Aoki, W., Beers, T. C., Christlieb, N., et al. 2007, ApJ, 655, 492
Aoki, W., Norris, J. E., Ryan, S. G., Beers, T. C., & Ando, H. 2002b, ApJL, 576, L141
Aoki, W., Ryan, S. G., Norris, J. E., et al. 2002c, ApJ, 580, 1149
Baranne, A., Queloz, D., Mayor, M., et al. 1996, A&AS, 119, 373
Barbuy, B., Spite, M., Spite, F., et al. 2005, A&A, 429, 1031
Bartkevicius, A. 1996, BaltA, 5, 217
Battino, U., Pignatari, M., Ritter, C., et al. 2016, ApJ, 827, 30
Beers, T. C., & Christlieb, N. 2005, ARA&A, 43, 531
Behara, N. T., Bonifacio, P., Ludwig, H.-G., et al. 2010, A&A, 513, A72
Bisterzo, S., Gallino, R., Käppeler, F., et al. 2015, MNRAS, 449, 506
Bisterzo, S., Gallino, R., Straniero, O., Cristallo, S., & Käppeler, F. 2010, MNRAS, 404, 1529
Bisterzo, S., Gallino, R., Straniero, O., Cristallo, S., & Käppeler, F. 2011, MNRAS, 418, 284
Bisterzo, S., Gallino, R., Straniero, O., Cristallo, S., & Käppeler, F. 2012, MNRAS, 422, 849
Busso, M., Gallino, R., & Wasserburg, G. J. 1999, ARA&A, 37, 239
Campbell, S. W., & Lattanzio, J. C. 2008, A&A, 490, 769
Chieffi, A., Limongi, M., & Straniero, O. 1998, ApJ, 502, 737
Christlieb, N., Green, P. J., Wisotzki, L., & Reimers, D. 2001, A&A, 375, 366
Cohen, J. G., Christlieb, N., Thompson, I., et al. 2013, ApJ, 778, 56
Cohen, J. G., McWilliam, A., Shectman, S., et al. 2006, AJ, 132, 137
Cowan, J. J., & Rose, W. K. 1977, ApJ, 212, 149
Cox, J. P., & Giuli, R. T. 1968, Principles of Stellar Structure (New York: Gordon and Breach)

Cristallo, S. 2006, PASP, 118, 1360
Cristallo, S., Abia, C., Straniero, O., & Piersanti, L. 2015a, ApJ, 801, 53
Cristallo, S., Piersanti, L., Straniero, O., et al. 2009a, PASA, 26, 139
Cristallo, S., Piersanti, L., Straniero, O., et al. 2011, ApJS, 197, 17
Cristallo, S., Straniero, O., Gallino, R., et al. 2009b, ApJ, 696, 797
Cristallo, S., Straniero, O., Lederer, M. T., & Aringer, B. 2007, ApJ, 667, 489
Cristallo, S., Straniero, O., Piersanti, L., & Gobrecht, D. 2015b, ApJS, 219, 40
Cui, W. Y., Sivarani, T., & Christlieb, N. 2013, A& A, 558, A36
Dardelet, L., Ritter, C., Prado, P., et al. 2015, arXiv:1505.05500
D'Orazi, V., Magrini, L., Randich, S., et al. 2009, ApJL, 693, L31
Fujimoto, M. Y., Ikeda, Y., & Iben, I., Jr. 2000, ApJL, 529, L25
Gallino, R., Arlandini, C., Busso, M., et al. 1998, ApJ, 497, 388
Goswami, A., & Aoki, W. 2010, MNRAS, 404, 253
Goswami, A., Aoki, W., Beers, T. C., et al. 2006, MNRAS, 372, 343
Goswami, A., Aoki, W., & Karinkuzhi, D. 2016, MNRAS, 455, 402
Hampel, M., Stancliffe, R. J., Lugaro, M., & Meyer, B. S. 2016, ApJ, 831, 171
Hansen, T. T., Andersen, J., Nordström, B., et al. 2016, A&A, 588, A3
Herwig, F. 2005, ARA&A, 43, 435
Herwig, F., Pignatari, M., Woodward, P. R., et al. 2011, ApJ, 727, 89
Herwig, F., Woodward, P. R., Lin, P.-H., Knox, M., & Fryer, C. 2014, ApJL, 792, L3
Hollek, J. K., Frebel, A., Placco, V. M., et al. 2015, ApJ, 814, 121
Hollowell, D., Iben, I., Jr., & Fujimoto, M. Y. 1990, ApJ, 351, 245
Ivans, I. I., Sneden, C., Gallino, R., Cowan, J. J., & Preston, G. W. 2005, ApJL, 627, L145
Iwamoto, N., Kajino, T., Mathews, G. J., Fujimoto, M. Y., & Aoki, W. 2004, ApJ, 602, 377
Johnson, J. A., & Bolte, M. 2004, ApJ, 605, 462
Jonsell, K., Barklem, P. S., Gustafsson, B., et al. 2006, A&A, 451, 651
Jorissen, A., Hansen, T., Van Eck, S., et al. 2016a, A&A, 586, A159
Jorissen, A., Van Eck, S., Van Winckel, H., et al. 2016b, A&A, 586, A158
Karakas, A. I., & Lattanzio, J. C. 2014, PASA, 31, 30
Karinkuzhi, D., & Goswami, A. 2014, MNRAS, 440, 1095
Karinkuzhi, D., & Goswami, A. 2015, MNRAS, 446, 2348
Lau, H. H. B., Stancliffe, R. J., & Tout, C. A. 2009, MNRAS, 396, 1046
Lebzelter, T., Uttenthaler, S., Straniero, O., & Aringer, B. 2013, A&A, 554, A30
Liu, G.-Q., Liang, Y.-C., & Deng, L.-C. 2009, RAA, 9, 431
Liu, N., Gallino, R., Bisterzo, S., et al. 2014a, ApJ, 788, 163
Liu, N., Savina, M. R., Davis, A. M., et al. 2014b, ApJ, 786, 66
Liu, N., Savina, M. R., Gallino, R., et al. 2015, ApJ, 803, 12
Liu, S., Nissen, P. E., Schuster, W. J., et al. 2012, A&A, 541, A48
Lu, K. 1991, AJ, 101, 2229
Lucatello, S. 2004, PhD thesis, Dipartimento di Astronomia, Univ. di Padova
Maiorca, E., Magrini, L., Busso, M., et al. 2012, ApJ, 747, 53
Maiorca, E., Randich, S., Busso, M., Magrini, L., & Palmerini, S. 2011, ApJ, 736, 120
Marigo, P. 2002, A&A, 387, 507
Marques, J. P., Goupil, M. J., Lebreton, Y., et al. 2013, A&A, 549, A74
Masseron, T., Johnson, J. A., Plez, B., et al. 2010, A&A, 509, A93
Mosser, B., Goupil, M. J., Belkacem, K., et al. 2012, A&A, 548, A10
Moultaka, J., Ilovaisky, S. A., Prugniel, P., & Soubiran, C. 2004, PASP, 116, 693
Noguchi, K., Aoki, W., Kawanomoto, S., et al. 2002, PASJ, 54, 855
Pereira, C. B., & Drake, N. A. 2009, A&A, 496, 791
Pereira, C. B., & Drake, N. A. 2011, AJ, 141, 79
Pereira, C. B., Jilinski, E., Drake, N. A., et al. 2012, A&A, 543, A58
Pereira, C. B., Sales Silva, J. V., Chavero, C., Roig, F., & Jilinski, E. 2011, A&A, 533, A51
Piersanti, L., Cristallo, S., & Straniero, O. 2013, ApJ, 774, 98
Placco, V. M., Frebel, A., Beers, T. C., et al. 2013, ApJ, 770, 104
Preston, G. W., & Sneden, C. 2001, AJ, 122, 1545
Roederer, I. U., Frebel, A., Shetrone, M. D., et al. 2008, ApJ, 679, 1549
Roederer, I. U., Preston, G. W., Thompson, I. B., et al. 2014, AJ, 147, 136
Roederer, I. U., Sneden, C., Thompson, I. B., Preston, G. W., & Shectman, S. A. 2010, ApJ, 711, 573
Ryan, S. G., Norris, J. E., & Beers, T. C. 1996, ApJ, 471, 254
Smiljanic, R., Porto de Mello, G. F., & da Silva, L. 2007, A&A, 468, 679
Smith, V. V., Coleman, H., & Lambert, D. L. 1993, ApJ, 417, 287
Sneden, C. A. 1973, PhD thesis, Univ. Texas
Sparks, W. M., & Endal, A. S. 1980, ApJ, 237, 130
Spruit, H. C. 2002, A&A, 381, 923
Stancliffe, R. J. 2010, MNRAS, 403, 505
Straniero, O., Gallino, R., Busso, M., et al. 1995, ApJL, 440, L85
Straniero, O., Gallino, R., & Cristallo, S. 2006, NuPhA, 777, 311
Thompson, I. B., Ivans, I. I., Bisterzo, S., et al. 2008, ApJ, 677, 556
Trippella, O., Busso, M., Palmerini, S., Maiorca, E., & Nucci, M. C. 2016, ApJ, 818, 125
Van Eck, S., Goriely, S., Jorissen, A., & Plez, B. 2003, A&A, 404, 291
Whitelock, P. A., Feast, M. W., van Loon, J. T., & Zijlstra, A. A. 2003, MNRAS, 342, 86
Woodward, P., Herwig, F., Porter, D., et al. 2008, in AIP Conf. Ser. 990, First Stars III, ed. B. W. O'Shea & A. Heger (Melville, NY: AIP), 300
Woodward, P. R., Herwig, F., & Lin, P.-H. 2015, ApJ, 798, 49
Začs, L., Schmidt, M. R., & Schuster, W. J. 2000, A&A, 358, 1022